

Heat-Treated Inconel 625 by Laser Powder Bed Fusion: Microstructure, Tensile Properties, and Residual Stress Evolution

*Original*

Heat-Treated Inconel 625 by Laser Powder Bed Fusion: Microstructure, Tensile Properties, and Residual Stress Evolution / Marchese, Giulio; Piscopo, Gabriele; Lerda, Serena; Salmi, Alessandro; Atzeni, Eleonora; Biamino, Sara. - In: JOURNAL OF MATERIALS ENGINEERING AND PERFORMANCE. - ISSN 1059-9495. - (2024). [10.1007/s11665-024-09235-7]

*Availability:*

This version is available at: 11583/2986550 since: 2024-03-04T20:59:35Z

*Publisher:*

SPRINGER

*Published*

DOI:10.1007/s11665-024-09235-7

*Terms of use:*

This article is made available under terms and conditions as specified in the corresponding bibliographic description in the repository

*Publisher copyright*

(Article begins on next page)



ORIGINAL RESEARCH ARTICLE

# Heat-Treated Inconel 625 by Laser Powder Bed Fusion: Microstructure, Tensile Properties, and Residual Stress Evolution

Giulio Marchese, Gabriele Piscopo, Serena Lerda, Alessandro Salmi, Eleonora Atzeni, and Sara Biamino

Submitted: 3 August 2023 / Accepted: 13 January 2024

This work investigates the impact of different heat treatments on the evolution of the microstructure, tensile properties, and residual stresses of Inconel 625 (IN625) processed by laser powder bed fusion (LPBF). Applying a heat treatment is an essential step to mitigate the high residual stresses in the components produced by LPBF and, simultaneously, to design the mechanical properties of the components. A high magnitude of residual stress can involve deformation and reduce the fatigue resistance of the components. In the current work, heat treatments performed at 600, 800, and 870 °C provided minimal modification on the dimensions of the grains but involved the formation of new phases, which increased the tensile strength. The results showed mitigation of the residual stresses at 800 and 870 °C correlated with the formation of Cr-rich  $M_{23}C_6$  carbides and  $\delta$  phases, respectively. Finally, the solution annealing at 1150 °C triggered recrystallization with the formation of sub-micrometric carbides, reducing the residual stresses. The solution annealing treatment involved an improvement of the ductility and a reduction in tensile strength. This work provides a guide to understanding the microstructure, residual stress, and mechanical properties evolution of the IN625 alloy under heat treatments.

**Keywords** additive manufacturing, inconel 625, laser powder bed fusion, microstructure, residual stress, superalloys

## 1. Introduction

Additive manufacturing laser powder bed fusion (LPBF) is progressively gaining attention for the possibility of fabricating complex components in a single step (Ref 1-4). This is particularly attractive for complex shape components made of Ni-based superalloys, where the LPBF process eliminates extensive subtractive processes that can be arduous due to their low machinability (Ref 5).

The Inconel 625 (IN625) represents one of the most employed laser powder bed fused (LPBFed) Ni-based superalloys due to its good weldability, which allows the production

of components with a low porosity (Ref 6-8). This superalloy offers high oxidation and corrosion protection up to around 1000 °C, combined with good fatigue resistance and tensile strength up to around 650 °C (Ref 9-12).

During the LPBF process, a laser beam melts the powder layer by layer, followed by a fast solidification, which creates a finer microstructure as well as high residual stresses inside the components. The originated residual stresses derived from the inherent high cooling rates of the LPBF process around  $10^5$ - $10^6$  K/s (Ref 7, 12). High level of residual stresses can also result in delamination, cracking, or distortion of the components. Finally, the residual stresses can reduce the mechanical performance and fatigue life of the components (Ref 13, 14).

These critical issues make it essential to study and determine the residual stresses in the LPBFed components. The main methods commonly used are x-ray diffraction, neutron diffraction, deformation methods, hole drilling test, and simulation methods (Ref 13, 15). X-ray diffraction and neutron diffraction use the variation of the crystalline structures in order to estimate the residual stresses (Ref 13). These methods allow the measurement of the residual stresses with a non-destructive procedure, and the principle is based on Bragg's law (Ref 16). X-ray diffraction has the great advantage that can be applied to a wide range of materials presenting high accuracy. However, the X-ray diffraction analysis is limited to small components, and the penetration is commonly lower than 0.1 mm. On the other hand, the neutron diffraction method has a high penetration of up to a few centimeters but requires high-cost equipment and zero-stress reference (Ref 16-18). The hole drilling test consists of drilling a hole in the center of a specimen, equipped with a grid strain gauge, in order to detect the redistribution of the strains for the residual stresses evaluation (Ref 19, 20). This method is widely used thanks

**Supplementary Information** The online version contains supplementary material available at <https://doi.org/10.1007/s11665-024-09235-7>.

**Giulio Marchese, Serena Lerda, and Sara Biamino**, Department of Applied Science and Technology, Politecnico di Torino, Corso Duca degli Abruzzi 24, 10129 Torino, Italy; and Interdepartmental Center of Integrated Additive Manufacturing (IAM@PoliTO), Politecnico di Torino, Corso Castelfidardo 51, 10129 Torino, Italy; and **Gabriele Piscopo, Alessandro Salmi, and Eleonora Atzeni**, Department of Management and Production Engineering, Politecnico di Torino, Corso Duca degli Abruzzi 24, 10129 Torino, Italy; and Interdepartmental Center of Integrated Additive Manufacturing (IAM@PoliTO), Politecnico di Torino, Corso Castelfidardo 51, 10129 Torino, Italy. Contact e-mail: [giulio.marchese@polito.it](mailto:giulio.marchese@polito.it).

to the measurement velocity and the possibility to evaluate the residual stresses up to around 1 mm, but it is a semi-destructive method (Ref 16, 17). Deformation methods like the cantilever method evaluate the deformation of parts to estimate the residual stresses but present low accuracy and the application are limited to simple shapes (Ref 21). Finally, simulation methods consider the thermomechanical properties of the material to estimate the residual stresses. However, the obtained results should be verified using one of the previous experimental referred methods (Ref 17, 18, 22).

The process parameters, scanning strategy, and the use of support structures could play a role in mitigating the residual stresses. Yi et al. (Ref 23) revealed that the increment in the laser power or the decrement in the scan speed could result in higher energy to the powder, thus generating more intense residual stresses inside Inconel 718 samples. However, the residual stress can be significantly mitigated by means of a subsequent heat treatment, which also influences the microstructure and mechanical performance in order to meet specific industrial requirements (Ref 24-28).

The purpose of stress relieving is to reduce the residual stress without drastically modifying the microstructure of the as-built condition. Another heat treatment is the solution annealing, which can involve recrystallization and chemical homogenization with the dissolution of formed phases. Finally, aging treatment provokes the formation of new strengthening phases (Ref 29, 30).

Currently, several studies are available on the residual stress evolution of the LPBFed Inconel 718. For instance, Deng et al. (Ref 24) assessed high residual stresses around 750-800 MPa for the as-fabricated conditions by X-ray diffraction analysis. The high residual stresses could be mitigated by the solution annealing (980 °C 1 h) plus aging treatment at (720 °C 8 h + 620 °C 8 h), thus reducing residual stresses by over 80 % compared to the initial conditions. Gruber et al. (Ref 31) reported that a solution annealing performed at 1150 °C for 6 h eliminated the residual stresses while maintaining a low fraction of residual stresses for a solution annealing at 1065 °C for 1.5 h determined by the cantilever approach. Marchese et al. (Ref 32) showed that 800 °C could mitigate the residual stresses up to around 100-200 MPa starting from the as-built condition of around 600 MPa determined by the hole drilling methods. Moreover, this temperature did not promote the formation of the detrimental  $\delta$  phases. Differently, the standard heat treatment at 980 °C generated the  $\delta$  phases.

However, each Ni-based superalloy undergoes specific microstructure, mechanical properties, and residual stress evolution under heat treatments. Therefore, each LPBFed Ni-based alloy requires a specific investigation.

In fact, few investigations on the LPBFed IN625 alloy examine the impact of heat treatments on the residual stresses combined with the microstructure. Lass et al. (Ref 27) showed that stress relieving at 800 °C for 1 h could mitigate residual stress, reaching values similar to the standard stress relieving at 870 °C for 1 h, determined using neutron diffraction. The lower stress relieving at 800 °C also effectively inhibited or reduced the formation of  $\delta$  phases for the standard stress relieving (Ref 26, 27, 33, 34). Moreover, Martucci et al. (Ref 35) reported that stress relieving at 750 °C and 800 °C started reducing the deflection of cantilever specimens due to the mitigation of residual stress. The residual stress was evaluated on the surface of the specimens using X-ray diffraction.

However, there is still lack of studies about the residual stresses of the heat-treated LPBFed IN625 on the surface and inside the material and correlate them to its microstructure and mechanical performance. The current work investigates the trend of the residual stress mitigation with the temperature for the LPBFed IN625 alloy. The microstructure and mechanical properties of LPBFed IN625 specimens are correlated with the residual stresses under different heat treatments. Heat treatments at 600, 800, 870, and 1150 °C were performed to shed light on the microstructure, tensile properties, and residual stresses evolution.

## 2. Materials and Methods

### 2.1 Specimens Production

The argon atomized powder of IN625 was supplied by EOS GmbH, and the nominal chemical composition is provided in Table 1.

The SEM image of the powder and its particle size distribution are shown in Fig. 1(a) and (b), respectively. The powder was composed of almost spherical particles with a d10 of 16  $\mu\text{m}$ , a d50 of 27  $\mu\text{m}$ , and a d90 of 40  $\mu\text{m}$ . The SEM micrograph shows particles covered by satellites and a few irregular particles, as commonly reported for the gas-atomized powder.

Cubic samples with dimensions of 10 × 10 × 10 mm<sup>3</sup> and 20 × 20 × 15 mm<sup>3</sup> and cylindrical samples with a length of 140 mm and diameter of 10 mm were produced by means of an EOS M270 dual mode version with a laser spot of 0.1 mm.

The first set of cubes was used to study the microstructure, while the second one was used to evaluate the residual stresses by means of the hole drilling test. The cylindrical samples were machined for the production of tensile specimens under the specification of the ASTM E8/E8M-22 (Ref 36). After machining, the specimens presented a gauge length of 40 mm and a diameter of 8 mm, consistent with the ASTM E8/E8M-22 (Ref 36).

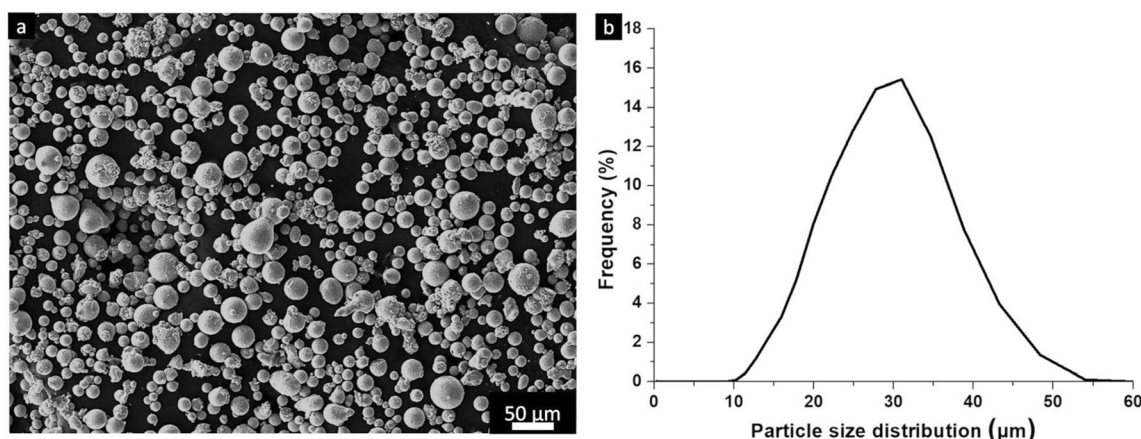
The selected process parameters were laser power of 195 W, hatching distance of 0.09 mm, a scanning speed of 1200 mm/s, and layer thickness of 0.02 mm. The scanning strategy consists of a laser scanning rotation of 67° using stripes of 5 mm. These process parameters were used in order to minimize the residual defects, as reported in a previous study by some of the authors (Ref 37).

Different heat treatments were performed on the as-built cubes and cylindrical specimens.

- A stress relieving at 600 °C for 1 h followed by air cooling. The temperature of 600 °C was selected based on the time-temperature-transformation (T-T-T) diagram of the IN625 alloy, highlighting that this temperature should avoid the formation of the detrimental  $\delta$  phase (Ref 9, 33).
- A stress relieving at 800 °C for 1 h followed by air cooling. This stress relieving is already proposed for the LPBFed IN625 since it avoids the formation of coarse  $\delta$  phases (Ref 33).
- A stress relieving at 870 °C for 1 h, followed by air cooling. This heat treatment is commonly used for the traditional processed IN625 alloy. However, the literature on

**Table 1** Chemical composition in weight percentage of the atomized IN625 powder

Ni	Cr	Mo	Fe	Nb	Co	Si	Ti	Al	C
≥ 58.0	20-23	8-10	≤ 5	3.15-4.15	≤ 1.0	≤ 0.5	≤ 0.4	≤ 0.4	≤ 0.1

**Fig. 1** (a) SEM image of the IN625 particles and (b) particle size distribution of the powder

LPBFed IN625 showed an accelerated formation of  $\delta$  phase formation (Ref 26, 29, 33).

- A solution annealing treatment was carried out at 1150 °C for 2 h, followed by air cooling. This heat treatment is indicated to homogenize the microstructure for the traditional processed IN625 alloy (Ref 29).

All the heat treatments were performed in a tubular furnace in air using a heating rate of 10 °C/min to reach the target temperature.

## 2.2 Microstructure and Mechanical Characterizations

The cubic samples with size  $10 \times 10 \times 10 \text{ mm}^3$  were cut along the building direction and then polished up to  $1 \text{ }\mu\text{m}$  with diamond suspension, followed by final polishing with alumina suspension ( $0.04 \text{ }\mu\text{m}$ ). Microstructure examination was carried out by light optical microscope (LOM—Leica DMI 5000 M), scanning electron microscope (SEM—Phenom XL) equipped with energy dispersive x-ray spectroscopy (EDS) unit, and (SEM—TESCAN S9000G) equipped with electron backscatter diffraction (EBSD) unit.

For the observation of the phases, the as-built and heat-treated samples were etched with mixed acid (15 ml HCl, 10 ml  $\text{CH}_2\text{COOH}$ , and 10 ml  $\text{HNO}_3$ ), while the final polished samples were employed for the grain texture analysis by EBSD. The EBSD analysis measurements were performed using a tilting angle of  $70^\circ$  scanned at 20 kV and 10 nA along the building direction using a step size between 1 and  $2 \text{ }\mu\text{m}$  covering an area of  $700 \times 650 \text{ }\mu\text{m}^2$  for each sample. Low-angle grain boundaries (LAGBs) were considered between  $2^\circ$  and  $10^\circ$ , while the high-angle grain boundaries (HAGBs) were considered  $> 10^\circ$ .

After machining, the tensile specimens were carried out by a Zwick-Roell BT1—FR100 testing machine at room temperature using a strain rate of  $8.10^{-3} \text{ s}^{-1}$  in agreement with the ASTM E8/E8M-22 standard (Ref 36), using three tensile

specimens for each condition. The cylinders used for the tensile specimens were produced orientated along the building direction (z-axis).

## 2.3 Residual Stresses Measurements

The residual stresses were measured using the hole drilling strain gage method. In this work, the MTS3000 (RESTAN) drilling machine equipped with an air turbine was used. A drill cutter with a diameter of 1.8 mm was used to produce a flat bottom hole in the analyzed surface. In detail, a 1.2-mm-depth hole was produced through a sequence of 24 steps of  $50 \text{ }\mu\text{m}$  each. Every drilling step caused material removal and, consequently, stress redistribution and relieved strains of the surrounding material. Then, at each step, the relieved strains were acquired on the analyzed surface by the strain gauge rosette previously installed, and strain values were used for the computation of the residual stress distribution according to the ASTM E837-20 standard (Ref 38). Specifically, relieved strains were acquired using a type B rosette (1-RY61-1.5/120R3-HBM). A detailed description of the procedure performed for stress evaluation is reported in (Ref 19, 25, 32). The stress profile through the depth was then described in terms of maximum and minimum principal stresses ( $\sigma_{\text{max}}$  and  $\sigma_{\text{min}}$ ) and the direction of the maximum principal stress with respect to gage 1 ( $\beta$ ).

## 3. Results and Discussion

### 3.1 Grains and Texture Evolution

Columnar grains can be detected for the as-built and stress-relieved conditions up to 870 °C (Fig. 2). The grain texture highlighted a high level of LAGBs (around 60-56%) for these conditions. The high quantity of LAGBs indicates a high level



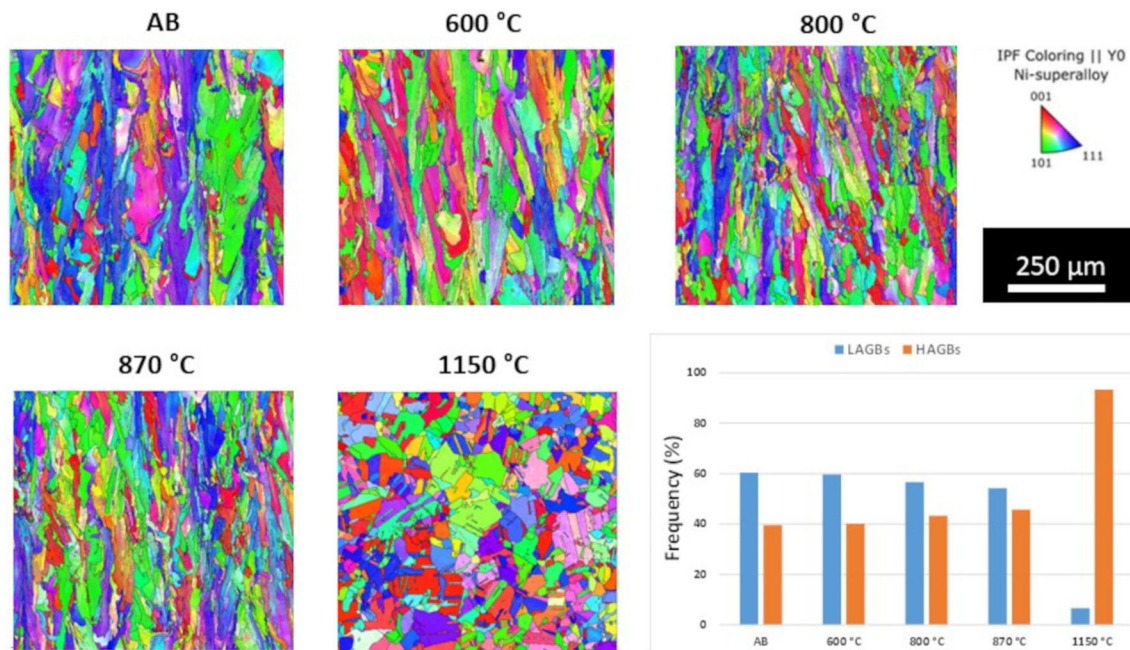


**Fig. 2** Inverse pole figure (IPF) maps of the IN625 in the as-built and heat-treated conditions along the building direction. The frequency of the LAGBs and HAGBs is reported in the graph

of an array of dislocation densities originated by the fast cooling rate of the process. The temperature increment was not high enough to activate the recrystallization for thermal exposure up to 870 °C. In fact, it was possible to observe only a slight decrement in the LAGBs from 600 to 870 °C.

Differently, solution annealing at 1150 °C triggered the recrystallization with a significant reduction in the LAGBs that dropped to around 7%. Recrystallization is commonly associated with a substantial reduction in residual stresses (Ref 31). In this case, the residual stresses and the high concentration of LAGBs can be the driving force for the recrystallization activation under the solution annealing temperature.

Regarding the grain size, the grains in the as-built and stress-relieved conditions presented lengths around 200 μm and widths around 20-30 μm, while the solution-annealed conditions presented equiaxed grains mainly ranging from 10 to 90 μm.

### 3.2 Microstructure Evolution

The microstructure of the as-built and 600 °C conditions appeared similar to each other by means of the LOM and SEM investigations. From the micrographs (Fig. 3a and b), it is possible to observe the melt pool contours and the columnar grains orientated along the building direction. High-magnification views (Fig. 3c, d, e, and f) show the sub-micrometric dendritic and cellular architectures generated by the fast cooling rates of the LPBF process. It is, therefore, evident that a thermal exposure at 600 °C for 1 h did not provoke the formation of coarse phases.

Likewise, the stress relieving at 800 and 870 °C did not alter the columnar grains, and the melt pool contours originated in the as-built state (Fig. 4a and b). The stress relieving at 800 and 870 °C, on the other hand, started to involve the formation of small carbides (indicated by red arrows) and δ phases, respectively. In both the stress-relieved conditions, the precip-

itates were mainly located along the grain boundaries and interdendritic areas (Fig. 4c and d).

For the 800 °C state, these carbides presented dimensions from sub-micrometric to a few microns (Fig. 4e), and the EDS analysis revealed enrichment in C and Cr, suggesting the formation of Cr-rich  $M_{23}C_6$  carbides, as pointed out in the supplementary (Ref 10). Differently, for the 870 °C condition, the δ phases presented the largest size up to a few microns along the grain boundaries, while the interdendritic areas chiefly exhibited sub-micrometric δ phases (Fig. 4f). Moreover, an initial dissolution of the dendritic/cellular structures appeared to occur under this temperature, as observed in a previous investigation (Ref 37). The δ phase identification is supported by its morphology and the enrichment in Ni and Nb, which was determined by EDS analysis, as reported in the supplementary (Ref 10, 39).

The δ phase tends to form mainly along the grain boundaries and interdendritic areas due to the solute trapping generated during the solidification, leading to the enrichment of Nb in these areas (Ref 12, 26). For this reason, the standard stress relieving provoked the formation of δ phases for shorter times with respect to the traditional stress-relieved IN625 alloy. This behavior is also highlighted by other studies in the literature (Ref 26, 33, 34, 40).

These results show how a lower temperature allows the limited formation of large phases inside the Ni-based superalloys, thus providing less macroscopical microstructure variations compared to the standard stress relieving heat treatments performed at 870 °C for 1 h. From the SEM analysis, no signals of the formation of δ phases were noted at 800 °C.

However, it should be noted that some studies reported that a stress relieving at 800 °C for 1 h already involved the formation of extremely low concentrations of δ phases (Ref 26, 33). The early formation of δ phases could be influenced by the slightly different chemical composition of the starting powder and the process parameters used. Moreover, applying different

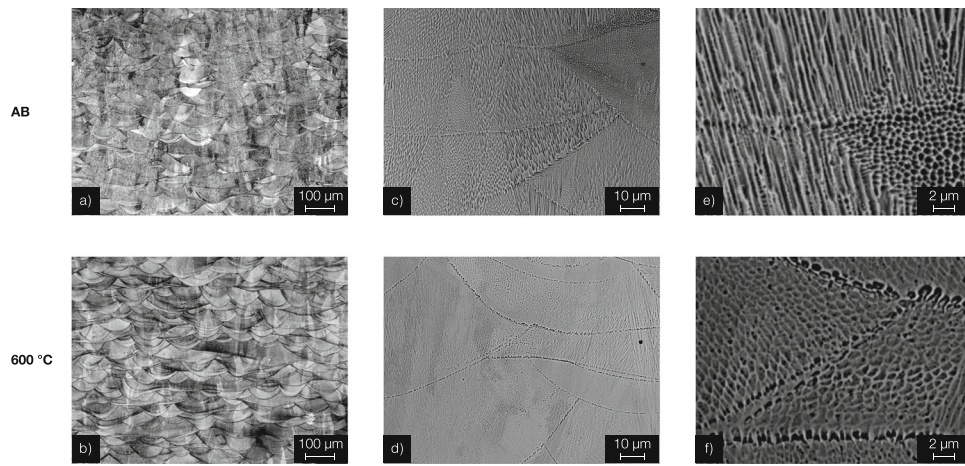


**Fig. 3** LOM (a,b) and SEM (c-f) images of the as-built and stress-relieved IN625 samples at 600 °C 1 h at different magnifications

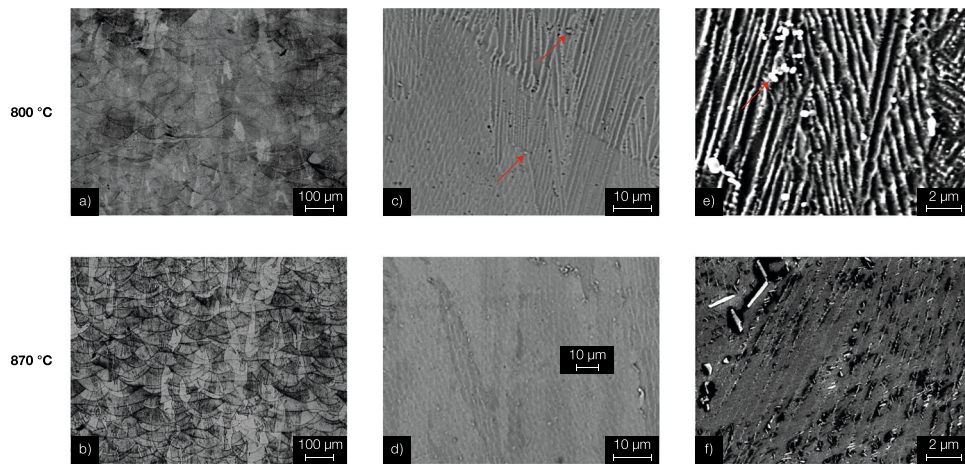


**Fig. 4** LOM (a,b) and SEM (c-f) images of the stress-relieved samples at 800 and 870 °C at different magnifications. The red arrows show precipitates

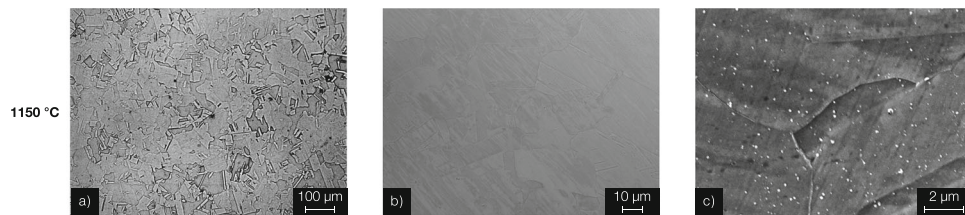


**Fig. 5** LOM (a) and SEM (b,c) images of the solution-annealed samples at 1150 °C 2 h at different magnifications

heat treatment parameters, like the heating and cooling rates, could also play a role in accelerating or decelerating the formation of the phases.

After the solution annealing at 1150 °C 2 h, the IN625 denoted the elimination of the columnar grains with the formation of equiaxed grains as well as the dissolution of the melt pools and dendritic architectures (Fig. 5a and b). High-magnification views display the formation of sub-micrometric carbides (around 100-300 nm) scattered throughout the samples (Fig. 5c). The absence of dendritic structures was generated by the complete homogenization of the chemical composition involved at high temperatures. These results are in line with other studies performed on high-temperature solution

annealing treatment (Ref 30, 37, 41). In this case, after the solution annealing the cooling rate is crucial to determine the dimensions of the carbides, and slower cooling rates could provoke the formation of larger carbides (Ref 12).

### 3.3 Mechanical Properties

The tensile properties highlight that the stress relieving at 600, 800, and 870 °C involved an increment in the yield strength (YS) and ultimate tensile strength (UTS) with a reduction in the elongation at failure compared to the as-built conditions, as reported in Table 2.



**Table 2 Tensile properties of the LPBFed IN625 specimens in the AB and stress-relieved and solution-annealed conditions built along the building direction (z-axis). The tensile properties are abbreviated as yield strength (YS), ultimate tensile strength (UTS), and elongation at break ( $\epsilon$ )**

Condition	YS, MPa	UTS, MPa	$\epsilon$ , %
AB (37)	618 $\pm$ 33	891 $\pm$ 5	41 $\pm$ 1
600, °C	775 $\pm$ 4	1033 $\pm$ 6	31 $\pm$ 2
800, °C	807 $\pm$ 6	1057 $\pm$ 6	29 $\pm$ 2
870, °C	715 $\pm$ 5	1017 $\pm$ 6	35 $\pm$ 4
1150, °C	430 $\pm$ 6	881 $\pm$ 3	53 $\pm$ 4

The ductility was remarkably depressed for the specimens heat-treated at 600 and 800 °C. From the results, it is possible to infer that the formation of phases, mostly like  $\gamma''$  phases and carbides, can play an essential role in strengthening the material while reducing its elongation at failure. For these two heat-treated conditions, the grains still presented a columnar shape, with a concentration of LAGBs similar to the as-built condition, and therefore, the formation of new phases appeared to be the predominant mechanism that enhanced the tensile strengths and reduced the ductility.

On the one hand, the stress-relieved 870 °C condition presented an initial dissolution of dendritic structures, increasing the ductility. However, the formation of  $\delta$  phases caused a ductility reduction. The sum of these two contributions induced an average ductility slightly inferior to the as-built condition. However, applying a more rapid cooling rate could limit the presence of  $\delta$  phases, thus resulting in higher ductility. Differently, the solution annealing treatment at 1150 °C for 2 h provided the lowest YS and UTS together with the highest elongation at failure with respect to the other heat-treated conditions. This result was originated by the fully dendritic structure dissolutions coupled with the elimination of the LAGBs.

Comparing the results with the literature, it is reported that the standard stress relieving at 870 °C can provide mechanical properties similar to the as-built state when followed by rapid cooling or water quenching when processed along the building direction (Ref 37, 42). Moreover, it is reported that a slightly higher temperature at 900 °C for 1 h resulted in lower YS but higher ductility with respect to the as-built state (Ref 43). Therefore, it is essential to consider all the heat treatment parameters, and consequently, also take into account the heating and cooling rates in order to determine the mechanical performance. Moreover, the mechanical properties deviations could derive from different initial microstructures induced by applying different process parameters.

The solution annealing treatment at 1150 °C for 2 h eliminated the mechanical anisotropy by forming equiaxed grains after recrystallizing, as reported in another study by some of the authors (Ref 37). In this case, the solution annealed samples followed by air cooling pointed out higher tensile strengths and compatible elongation at failure with a larger standard deviation with respect to the solution annealed sample followed by water quenching. This difference can be attributed to the greater formation of carbides during the cooling steps. In fact, the water quenching inhibits the further formation or

growth of carbides during the cooling step. Moreover, the tensile properties of the solution annealed samples were close to the LPBFed IN625 samples that underwent 1100 °C for 1 h, followed by air cooling reported in another study (Ref 43). Gonzalez et al. (Ref 44) performed a HIP treatment at around 1160 °C 3 h 102 MPa on IN625 LPBFed samples, reporting slightly lower tensile strengths and compatible elongation with the current solution annealed specimens, considering specimens built along the building direction. In this last case, the differences can be attributed to the slightly higher temperature and prolonged heat treatment times.

### 3.4 Fracture Surface Analyses

The SEM fracture surfaces of tensile specimens are illustrated in Figure 6. The fracture surface of the as-built sample showed a ductile fracture mode with dimples and microvoids as well as brittle fracture areas characterized by smooth zone, probably induced by the presence of segregations in the interdendritic areas. The fracture surface morphology results to be similar to the typical fracture surface of the LPBFed IN625 alloy (Ref 44). In the case of stress-relieved samples at 600 and 800 °C, the samples still presented ductile and brittle surfaces. The smooth zones of the cleavage pattern are most likely derived from the  $\gamma''$  phases and Cr-rich  $M_{23}C_6$  carbides for the 600 and 800 °C states, respectively. In fact, it is known that the formation of reinforced phases enhances the tensile strength of the alloy, but these phases also create new weaker spots for the formation of a cleavage pattern (Ref 45).

Likewise, the 870 °C condition presented mixed ductile and brittle fractures, where the formation of the micrometric  $\delta$  phase induced the creation of brittle fracture, while the initial dendritic dissolution appeared to favor ductile fracture mechanisms.

Differently, the solution annealed condition is characterized by a more marked ductile fracture mode with microvoids coalescence, showing pores with dimensions also around 50-80  $\mu$ m, while the as-built and the other heat-treated conditions exhibited fracture surfaces with pores around 10-20  $\mu$ m. In this case, the larger size of microvoids created during the plastic deformation implies a superior ductility originated by the dissolution of the dendritic structures with the strong mitigation of the LAGBs.

### 3.5 Residual Stresses

Figures 7 and 8 show the distribution and the direction of the principal residual stresses measured on the top and the lateral surfaces of the samples subjected to different heat treatments. For better clarity, the stress profiles on top (Fig. 7) and lateral (Fig. 8) surfaces are presented in two sub-figures, combining results from as-built samples and samples heat-treated at 600 °C (Fig. 7a and 8a), and results from heat-treated samples from 800 to 1150 °C (Fig. 7b and 8b).

The as-built sample is characterized by a tensile stress state on both the top and the lateral surfaces. On the top surface (Fig. 7a), a sub-surface value of about 100 MPa was measured. Then, the stress reached a maximum value of 500 MPa around 0.4 mm. Subsequently, the stress slightly oscillated, reaching a local minimum of about 370 MPa at a distance of 0.7 mm from the surface, increasing up to 490 MPa at the maximum measured depth. The stress measured on the lateral surfaces reported higher values. The value of the sub-surface maximum principal stress on the lateral surface (Fig. 8a) was 650 MPa.

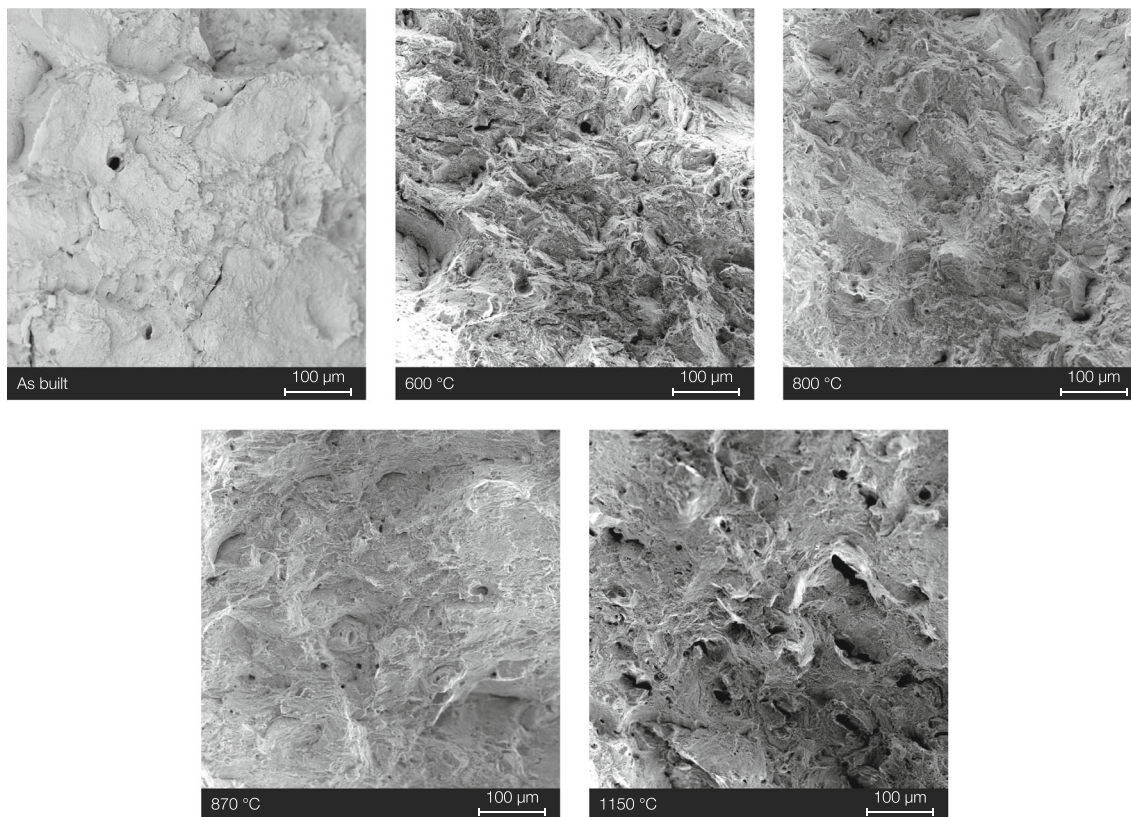


**Fig. 6** SEM images of fracture surfaces of tensile IN625 specimens in the as-built and different heat-treated conditions

Likewise, the stress distribution was characterized by an oscillating trend. The stress reached its maximum value of 780 MPa at a depth of 0.6 mm, then the stress decreased up to a local minimum of 340 MPa at a depth of 0.85 mm.

The heat treatment at 600 °C did not significantly modify the stress mean value, even if it highly strengthens the oscillatory trend of the stress distribution. On the other hand, on the lateral surface of the sample heat-treated at 600 °C, a significant reduction in residual stress value from 780 to 450 MPa was observed.

The beta angle, which measures the principal direction, showed that on the top surface (Fig. 7), the plane of principal stresses sharply varies along the analyzed depth as the oscillation begins, and it ranges between  $-90^\circ$  and  $90^\circ$ . Conversely, on the lateral surface (Fig. 8), the value of the principal direction smoothly decreased from about  $-40^\circ$  to  $-55^\circ$ . On the lateral surfaces, the beta angle mean value was about  $-45^\circ$ , indicating that the maximum principal stress was oriented parallel to the columnar grains (and so along the building direction). On the other hand, on the top surface, the direction varied since the grain morphology was randomly distributed.

The heat treatments from 800 to 1150 °C caused a significant reduction in residual stress values. From Fig. 7(b) and 8(b), it is possible to observe that increasing the temperature from 600 to 870 °C resulted in a reduction in residual stress value. The measured maximum principal stress decreased from 600 to 340 MPa. It is essential to point out that no remarkable differences were observed between the heat treatment at 800 °C and the standard stress relieving at 870 °C, conventionally used for Inconel 625 alloy. In both cases, the

measured residual stress ranges between 0 and 300 MPa. Interestingly, heat-treated samples at 1150 °C slightly increased the residual stress, reaching 360 MPa at around 0.4 mm. Furthermore, at a depth of around 0.6 mm, the residual stress changed from a tensile to a compressive stress state. This behavior could be attributed to the formation of carbides, which caused a modification of residual stress status. In addition, as observed in Fig. 7(b) and 8(b), the direction of the maximum principal stress showed a highly variable distribution. The maximum principal stress was about  $-45^\circ$ , resulting in the direction parallel to the columnar grains for the sample heat-treated at 800 °C. Conversely, the heat-treated samples at 870 and 1150 °C reported pronounced variations of the beta angle that could be attributed to the formation of coarse precipitates and recrystallization mechanisms, respectively.

Overall, the stress relieving at 800 and 870 °C underlined mitigation of the residual stresses. The stress relieving at 800 °C appeared to inhibit the formation of micrometric  $\delta$  phases but caused the formation of  $\text{Cr-M}_{23}\text{C}_6$  carbides that could increase the susceptibility to intergranular corrosion. Finally, the solution annealing treatment at 1150 °C showed areas with residual stress increment probably due to the formation of a large fraction of carbides, which can locally raise the stress inside the material.

## 4. Conclusions

The LPBFed IN625 alloy presents a fine microstructure due to fast cooling rates, which generate high mechanical performance. However, the high cooling rates of the LPBF process



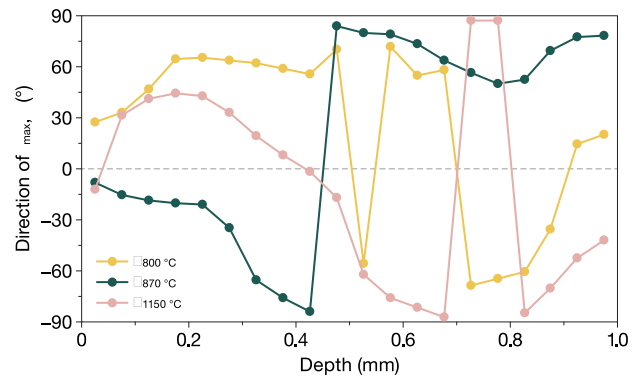
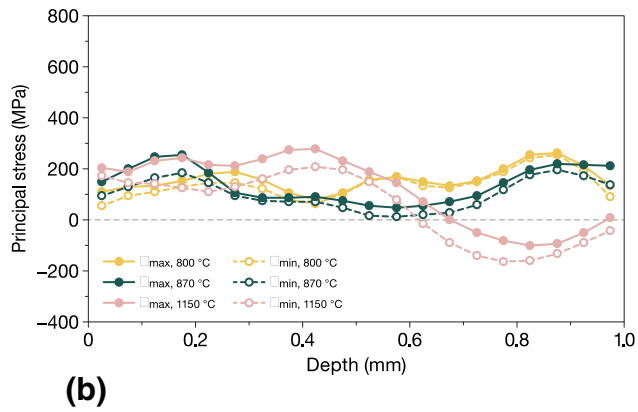
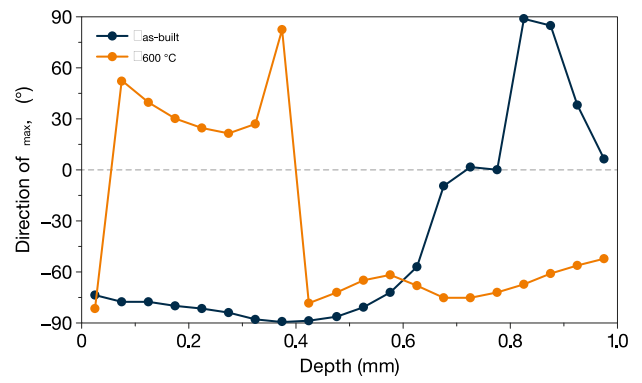
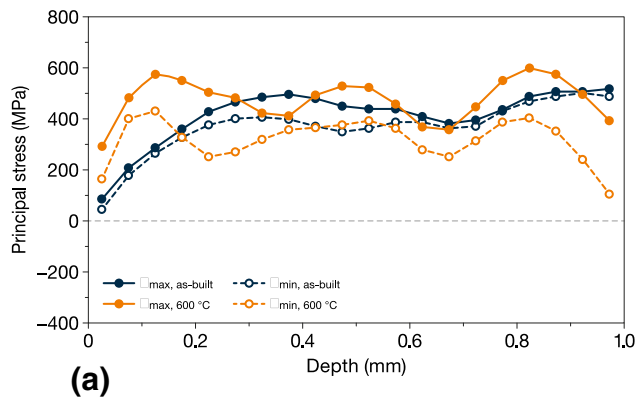


**Fig. 7** Residual stress distribution and principal stress direction measured on the top surface of samples with different conditions: (a) as-built and 600 °C and (b) 800, 870 and 1150 °C

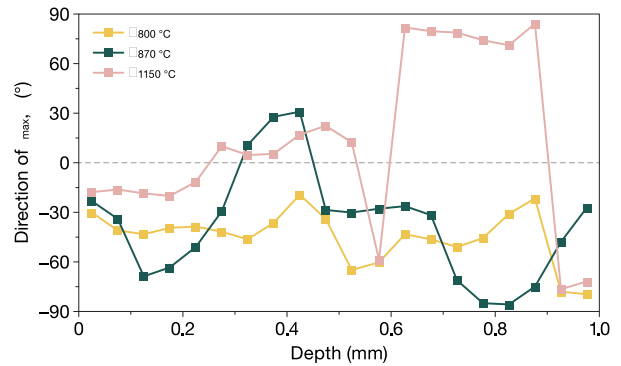
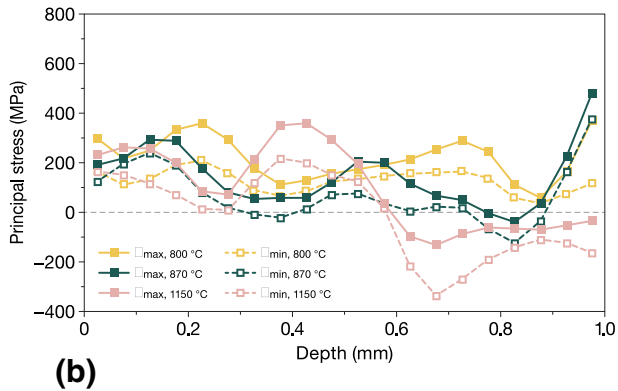
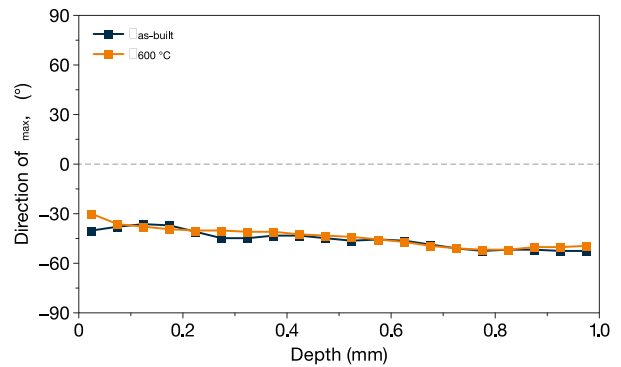
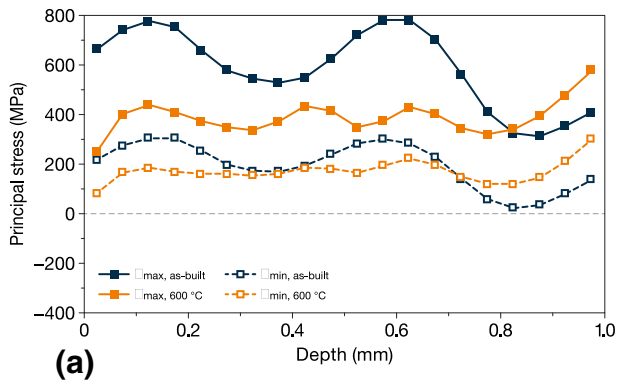


**Fig. 8** Residual stress distribution and principal stress direction measured on the lateral surface of samples with different conditions: (a) as-built and 600 °C and (b) 800, 870 and 1150 °C

also produce high residual stresses that could create distortion on the components.

A possible strategy to mitigate the residual stresses is the application of heat treatments. The current study determines the evolution of the microstructure, mechanical performance, and residual stresses from the surface and inside the material under different heat treatments.

The main conclusions of this investigation are:

- The as-built and stress-relieved samples at 600 °C presented similar microstructure, level of LAGBs, and magnitude of residual stress. However, the stress-relieved samples at 600 °C presented higher tensile strength and lower ductility with respect to the as-built condition. The variations in mechanical properties could be ascribed to the possible formation of nanometric phases.
- Stress relieving at 800 and 870 °C showed the same characteristic columnar grains of the as-built condition with similar concentration of LAGBs, but the temperatures were effective in mitigating the residual stress. Heat treatments at 800 °C showed the formation of Cr-rich  $M_{23}C_6$  carbides, while 870 °C generated  $\delta$  phases. The tensile properties reported high tensile strengths but lower ductility with respect to the as-built condition. The ductility reduction was less pronounced for the samples stress-relieved at 870 °C, probably due to the initial dendritic dissolution, which promoted ductility improvement, thus mitigating the brittle effect of the  $\delta$  phase.
- The solution annealed samples at 1150 °C showed recrystallization with a strong reduction in LAGBs, residual stress mitigation with the local rise of stress, and dissolution of the dendritic structures. In this state, the material presented the highest ductility and the lowest tensile strength among the tested conditions.

This work shows the variation of the microstructure, tensile properties, and residual stresses of the as-built and different heat-treated conditions. The results provide a useful guide to understanding the evolution of the residual stresses in the LPBFed IN625 alloy.

## Funding

Open access funding provided by Politecnico di Torino within the CRUI-CARE Agreement.

## Conflict of interest

The authors declare that they have no known competing financial interests or personal relationships that could have appeared to influence the work reported in this paper.

## Open Access

This article is licensed under a Creative Commons Attribution 4.0 International License, which permits use, sharing, adaptation, distribution and reproduction in any medium or format, as long as you give appropriate credit to the original author(s) and the source, provide a link to the Creative Commons licence, and indicate if changes were made. The images or other third party material in this

article are included in the article's Creative Commons licence, unless indicated otherwise in a credit line to the material. If material is not included in the article's Creative Commons licence and your intended use is not permitted by statutory regulation or exceeds the permitted use, you will need to obtain permission directly from the copyright holder. To view a copy of this licence, visit <http://creativecommons.org/licenses/by/4.0/>.

## References

1. E. Herderick, Additive Manufacturing of Metals: A Review, *Mater. Sci. Technol. Conf. Exhib.*, 2011, **2**(176252), p 1413–1425.
2. D.D. Gu, W. Meiners, K. Wissenbach, and R. Poprawe, Laser Additive Manufacturing of Metallic Components: Materials, Processes and Mechanisms, *Int. Mater. Rev.*, 2012, **57**(3), p 133–164.
3. W.E. King, A.T. Anderson, R.M. Ferencz, N.E. Hodge, C. Kamath, S.A. Khairallah, and A.M. Rubenchik, Laser Powder Bed Fusion Additive Manufacturing of Metals: Physics, Computational, and Materials Challenges, *Appl. Phys. Rev.*, 2015, **2**(4), p 041304. <https://doi.org/10.1063/1.4937809>
4. W.E. Frazier, Metal Additive Manufacturing: A Review, *J. Mater. Eng. Perform.*, 2014, **23**(6), p 1917–1928.
5. I.A. Choudhury and M.A. El-Baradie, Machinability of Nickel-Base Super Alloys: A General Review, *J. Mater. Process. Technol.*, 1998, **77**(1–3), p 278–284. [https://doi.org/10.1016/S0924-0136\(97\)00429-9](https://doi.org/10.1016/S0924-0136(97)00429-9)
6. L.N. Carter, M.M. Attallah, and R.C. Reed, Laser Powder Bed Fabrication of Nickel-Base Superalloys: Influence of Parameters; Characterisation, Quantification and Mitigation of Cracking, *Superalloys*, 2012, **2012**, p 577–586.
7. M.M. Attallah, R. Jennings, X. Wang, and L.N. Carter, Additive Manufacturing of Ni-Based Superalloys: The Outstanding Issues, *MRS Bull.*, 2016, **41**(10), p 758–764.
8. Z. Tian, C. Zhang, D. Wang, W. Liu, X. Fang, D. Wellmann, Y. Zhao, and Y. Tian, A Review on Laser Powder Bed Fusion of Inconel 625 Nickel-Based Alloy, *Appl. Sci.*, 2020, **10**(1), p 81.
9. S. Floreen, G.E. Fuchs, and W.J. Yang, The Metallurgy of Alloy 625, *Superalloys*, 1994, **718**(625), p 13–37.
10. L.M. Suave, J. Cormier, P. Villechaise, A. Soula, Z. Hervier, D. Bertheau, and J. Laigo, Microstructural Evolutions during Thermal Aging of Alloy 625: Impact of Temperature and Forming Process, *Metall. Mater. Trans. A Phys. Metall. Mater. Sci.*, 2014, **45**(7), p 2963–2982.
11. H.L. Eiselstein and D.J. Tillack, The Invention and Definition of Alloy 625, *Superalloys*, 1991, **718**(625), p 1–14.
12. S. Li, Q. Wei, Y. Shi, Z. Zhu, and D. Zhang, Microstructure Characteristics of Inconel 625 Superalloy Manufactured by Selective Laser Melting, *J. Mater. Sci. Technol.*, 2015, **31**(9), p 946–952. <http://doi.org/10.1016/j.jmst.2014.09.020>
13. J.L. Bartlett and X. Li, An Overview of Residual Stresses in Metal Powder Bed Fusion, *Addit. Manuf.*, 2019, **27**, p 131–149. <https://doi.org/10.1016/j.addma.2019.02.020>
14. P. Mercelis and J.P. Kruth, Residual Stresses in Selective Laser Sintering and Selective Laser Melting, *Rapid Prototyp J*, 2006, **12**(5), p 254–265.
15. C. Li, Z.Y. Liu, X.Y. Fang, and Y.B. Guo, Residual Stress in Metal Additive Manufacturing, *Proc. CIRP*, 2018, **71**, p 348–353.
16. G.S. Schajer, M.B. Prime, and P.J. Withers, Why Is It So Challenging to Measure Residual Stresses?, *Exp. Mech.*, 2022, **62**(9), p 1521–1530.
17. G.U.O. Jiang, F.U. Haiyang, P.A.N. Bo, and K.A.N.G. Renke, Recent Progress of Residual Stress Measurement Methods: A Review, *Chin. J. Aeronaut.*, 2021, **34**(2), p 54–78.
18. N.S. Rossini, M. Dassisti, K.Y. Benyounis, and A. Olabi, Methods of Measuring Residual Stresses in Components, *Mater. Design*, 2012, **35**, p 572–588.
19. A. Salmi and E. Atzeni, Residual Stress Analysis of Thin AlSi10Mg Parts Produced by Laser Powder Bed Fusion, *Virt. Phys. Prototyp.*, 2020, **15**(1), p 49–61. <https://doi.org/10.1080/17452759.2019.1650237>
20. A. Salmi, E. Atzeni, L. Iuliano, and M. Galati, Experimental Analysis of Residual Stresses on AlSi10Mg Parts Produced by Means of Selective Laser Melting (SLM), *Proc. CIRP*, 2017, **62**, p 458–463. <https://doi.org/10.1016/j.procir.2016.06.030>

21. F.A. Kandil, J.D. Lord, A.T. Fry,, and P. V Grant, A Review of Residual Stress Measurement Methods-A Guide to Technique Selection. By, 2001
22. Y. Yang, M. Allen, T. London, and V. Oancea, Residual Strain Predictions for a Powder Bed Fusion Inconel 625 Single Cantilever Part, *Integr. Mater. Manuf. Innov.*, 2019, **8**(3), p 294–304.
23. J.H. Yi, J.W. Kang, T.J. Wang, X. Wang, Y.Y. Hu, T. Feng, Y.L. Feng, and P.Y. Wu, Effect of Laser Energy Density on the Microstructure, Mechanical Properties, and Deformation of Inconel 718 Samples Fabricated by Selective Laser Melting, *J. Alloys Compd.*, 2019, **786**, p 481–488.
24. D. Deng, R.L. Peng, H. Brodin, and J. Moverare, Microstructure and Mechanical Properties of Inconel 718 Produced by Selective Laser Melting: Sample Orientation Dependence and Effects of Post Heat Treatments, *Mater. Sci. Eng. A*, 2018, **713**, p 294–306. <https://doi.org/10.1016/j.msea.2017.12.043>
25. R. Barros, F.J.G. Silva, R.M. Gouveia, A. Saboori, G. Marchese, S. Biamino, A. Salmi, and E. Atzeni, Laser Powder Bed Fusion of Inconel 718: Residual Stress Analysis before and after Heat Treatment, *Metals*, 2019, **9**(12), p 1290.
26. G. Lindwall, C.E. Campbell, E.A. Lass, F. Zhang, M.R. Stoudt, A.J. Allen, and L.E. Levine, Simulation of TTT Curves for Additively Manufactured Inconel 625, *Metall. Mater. Trans. A*, 2019, **50**(1), p 457–467. <https://doi.org/10.1007/s11661-018-4959-7>
27. E.A. Lass, M.R. Stoudt, M.E. Williams, M.B. Katz, L.E. Levine, T.Q. Phan, T.H. Gnaeupel-Herold, and D.S. Ng, Formation of the Ni3Nb  $\delta$ -Phase in Stress-Relieved Inconel 625 Produced via Laser Powder-Bed Fusion Additive Manufacturing, *Metall. Mater. Trans. A Phys. Metall. Mater. Sci.*, 2017, **48**(11), p 5547–5558.
28. Ó. Teixeira, F.J. Silva, and E. Atzeni, Residual Stresses and Heat Treatments of Inconel 718 Parts Manufactured via Metal Laser Beam Powder Bed Fusion: An Overview, *Int. J. Adv. Manuf. Technol.*, 2021, **113**(11–12), p 3139–3162. <https://doi.org/10.1007/s00170-021-06835-8>
29. M.J. Donachie and S.J. Donachie, *Superalloys: A Technical Guide*, ASM International, 2nd ed. ASM International, Materials Park, 2002
30. A. Kreitzberg, V. Brailovski, and S. Turenne, Effect of Heat Treatment and Hot Isostatic Pressing on the Microstructure and Mechanical Properties of Inconel 625 Alloy Processed by Laser Powder Bed Fusion, *Mater. Sci. Eng. A*, 2017, **689**, p 1–10. <https://doi.org/10.1016/j.msea.2017.02.038>
31. K. Gruber, R. Dziedzic, B. Kuźnicka, B. Madejski, and M. Malicki, Impact of High Temperature Stress Relieving on Final Properties of Inconel 718 Processed by Laser Powder Bed Fusion, *Mater. Sci. Eng. A*, 2021, **813**, p 141111.
32. G. Marchese, E. Atzeni, A. Salmi, and S. Biamino, Microstructure and Residual Stress Evolution of Laser Powder Bed Fused Inconel 718 under Heat Treatments, *J. Mater. Eng. Perform.*, 2021, **30**(1), p 565–574.
33. M.R. Stoudt, E.A. Lass, D.S. Ng, M.E. Williams, F. Zhang, C.E. Campbell, G. Lindwall, and L.E. Levine, The Influence of Annealing Temperature and Time on the Formation of  $\delta$ -Phase in Additively-Manufactured Inconel 625, *Metall. Mater. Trans. A*, 2018, **49A**, p 3028–3037.
34. F. Zhang, L.E. Levine, A.J. Allen, M.R. Stoudt, G. Lindwall, E.A. Lass, M.E. Williams, Y. Idell, and C.E. Campbell, Effect of Heat Treatment on the Microstructural Evolution of a Nickel- Based Superalloy Additive-Manufactured by Laser Powder Bed Fusion, *Acta Mater.*, 2018, **152**, p 200–214.
35. A. Martucci, G. Marchese, E. Bassini, and M. Lombardi, Effects of Stress-Relieving Temperature on Residual Stresses, Microstructure and Mechanical Behaviour of Inconel 625 Processed by PBF-LB/M, *Metals*, 2023, **13**(4), p 796. <https://doi.org/10.3390/met13040796>
36. ASTM international (2022) ASTM E8/E8M – 22 Standard Test Methods for Tension Testing of Metallic Materials. doi:[https://doi.org/10.1520/E0008\\_E0008M-22](https://doi.org/10.1520/E0008_E0008M-22)
37. G. Marchese, S. Parizia, M. Rashidi, A. Saboori, D. Manfredi, D. Ugues, M. Lombardi, E. Hryha, and S. Biamino, The Role of Texturing and Microstructure Evolution on the Tensile Behavior of Heat-Treated Inconel 625 Produced via Laser Powder Bed Fusion, *Mater. Sci. Eng. A*, 2020, **769**, p 138500. <https://doi.org/10.1016/j.msea.2019.138500>
38. ASTM International. ASTM E837- 20 Standard Test Method for Determining Residual Stresses by the Hole-Drilling Strain-Gage Method. 2020, doi:<https://doi.org/10.1520/E0837-20>
39. L.M. Suave, D. Bertheau, J. Cormier, P. Villechaise, A. Soula, Z. Hervier, and J. Laigo, Impact of Microstructural Evolutions during Thermal Aging of Alloy 625 on Its Monotonic Mechanical Properties, *MATEC Web Conf.*, 2014, **14**, p 21001.
40. E.A. Lass, M.R. Stoudt, M.B. Katz, and M.E. Williams, Precipitation and Dissolution of  $\delta$  and  $\Gamma''$  during Heat Treatment of a Laser Powder-Bed Fusion Produced Ni-Based Superalloy, *Scr. Mater.*, 2018, **154**, p 83–86. <https://doi.org/10.1016/j.scriptamat.2018.05.025>
41. K. Inaekyan, A. Kreitzberg, S. Turenne, and V. Brailovski, Microstructure and Mechanical Properties of Laser Powder Bed-Fused IN625 Alloy, *Mater. Sci. Eng. A*, 2019, **768**, p 138481. <https://doi.org/10.1016/j.msea.2019.138481>
42. EOS and EOS GmbH - Electro Optical Systems, “Material Data Sheet - EOS Nickel Alloy IN625,” 2011, p 1–5, <https://www.eos.info/materials-l-m>. Accessed 27 March 2019
43. J. Nguejio, F. Szmytka, S. Hallais, A. Tanguy, S. Nardone, and M.G. Martinez, Comparison of Microstructure Features and Mechanical Properties for Additive Manufactured and Wrought Nickel Alloys 625, *Mater. Sci. Eng. A*, 2019, **764**, p 138214.
44. J.A. Gonzalez, J. Mireles, S.W. Stafford, M.A. Perez, C.A. Terrazas, and R.B. Wicker, Characterization of Inconel 625 Fabricated Using Powder-Bed-Based Additive Manufacturing Technologies, *J. Mater. Process. Technol.*, 2017, **2018**(264), p 200–210. <https://doi.org/10.1016/j.jmatprotec.2018.08.031>
45. J. Mittra, S. Banerjee, R. Tewari, and G.K. Dey, Fracture Behavior of Alloy 625 with Different Precipitate Microstructures, *Mater. Sci. Eng. A*, 2013, **574**, p 86–93.

**Publisher's Note** Springer Nature remains neutral with regard to jurisdictional claims in published maps and institutional affiliations.